J Adv Ceram

Research Article

Ultrahigh voltage-gradient ZnO-based varistor ceramics via hybrid cold sintering process/spark plasma sintering and post-annealing process

Shenglin Kang[1], Xuetong Zhao[1,✉], Qi Wang[1], Jie Liang[1], Jing Guo[2], Xilin Wang[3], Guilai Yin[4], Lijun Yang[1], Ruijin Liao[1]

Cite this article: Kang S, Zhao X, Wang Q, et al. *J Adv Ceram* 2025, **14**(5): 9221065. https://doi.org/10.26599/JAC.2025.9221065

ABSTRACT: A high voltage gradient (V_g) of ZnO-based varistor ceramics is critical for realizing miniaturized and lightweight overvoltage protection devices. However, improving V_g of ZnO-based varistor ceramics through conventional high-temperature sintering process remains a significant challenge. Here, we present a strategy to fabricate ultrahigh voltage-gradient ZnO-based varistor ceramics by combining cold sintering process/spark plasma sintering (CSP–SPS) with post-annealing process. Employing CSP–SPS, the ZnO-based varistor ceramics were initially densified at 300 °C and subsequently annealed at a low temperature of 700–900 °C. CSP–SPS technique combined with a low annealing temperature enables the production of ZnO-based varistor ceramics with fine and homogeneous microstructures, while suppressing the volatilization of Bi-rich phases at grain boundaries. This approach achieves the ultrahigh V_g of ~1832.71 V/mm, high nonlinear coefficient (α) of ~106.69, and low leakage current density (J_L) of less than 0.2 μA/cm². This work shows that the integration of CSP–SPS and post-annealing provides a promising way to design ZnO-based varistor ceramics with ultrahigh V_g.

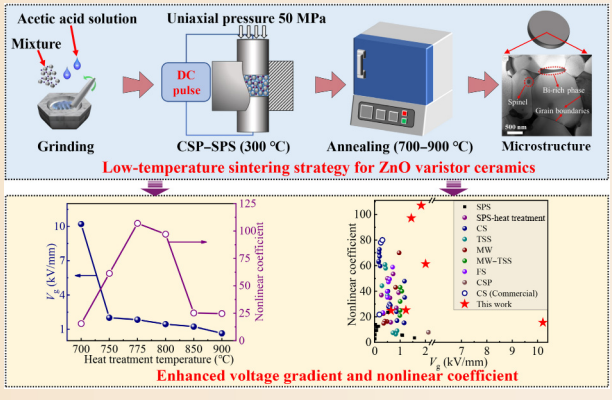

KEYWORDS: cold sintering process (CSP); spark plasma sintering (SPS); ZnO-based varistor ceramics; microstructure; voltage gradient

1 Introduction

ZnO-based varistor ceramics exhibit excellent nonlinear current–voltage characteristics and are widely used as the core component of metal oxide arresters (MOAs) for high-voltage power systems and surge pulse devices (SPDs) in low-voltage electronic circuits [1,2]. With the rapid development of extra-/ultrahigh voltage power transmission, ultrahigh voltage gradient ZnO-based varistor ceramics are highly desirable for overvoltage protection and insulation coordination [3]. Generally, the non-ohmic behavior of ZnO-based varistor ceramics is determined by double-Schottky barriers (DSBs) at the grain boundaries, which can be manipulated by dopants such as Bi_2O_3, Mn_2O_3, CoO, Sb_2O_3, and Cr_2O_3, as well as through sintering techniques. Recently, several types of rare-earth metal oxides (In_2O_3, Y_2O_3, etc.) have been introduced into ZnO-based varistor ceramics to enhance the voltage gradient (V_g) [4,5]. Incorporating rare-earth metal oxides effectively decreases the grain size of ZnO ceramics and achieves the enhanced V_g of 444 V/mm [5]. Alternatively, nano-sized ZnO powders have been used to regulate the grain size distribution, which improves V_g of ZnO varistors up to 803 V/mm [6]. However, a high sintering temperature (~1200 °C) and long soaking time are still required to densify green samples via conventional solid-state sintering technique, leading to significant energy loss, grain overgrowth, and volatilization of Bi-rich phase at grain boundaries [7,8].

In recent decades, rapid sintering techniques have emerged, including spark plasma sintering (SPS) [9,10], microwave sintering (MW) [11,12], flash sintering (FS) [13,14], ultrafast high-temperature sintering (UHS) [15], and cold sintering process (CSP). Specifically, since 2016, CSP has been extensively developed to densify ceramic materials at temperatures ranging from room temperature to 300 °C within a short sintering time

[1] State Key Laboratory of Power Transmission Equipment Technology, School of Electrical Engineering, Chongqing University, Chongqing 400044, China. [2] State Key Laboratory for Mechanical Behavior of Materials, School of Materials Science and Engineering, Xi'an Jiaotong University, Xi'an 710049, China. [3] Tsinghua University, Shenzhen 518055, China. [4] State Grid Jiangxi Electric Power Research Institute, Nanchang 330096, China.

✉ Corresponding author. E-mail: zxt201314@cqu.edu.cn

Received: December 31, 2024; Revised: February 27, 2025; Accepted: March 20, 2025

(from a few minutes to several hours) [16,17]. Typically, CSP refers to a mixture of ceramic powders and a suitable transient liquid phase (such as water, weak acids, or organic solutions) set in a die and heated under uniaxial pressure; thus, the densification of ceramics can be completed through a mediated dissolution–precipitation process at a temperature below 300 °C [18]. Recent studies show successful CSP densification of diverse ceramic materials, such as ZnO [19], $BaTiO_3$ [20], SiO_2 [21], and $Li_{1.5}Al_{0.5}Ge_{1.5}(PO_4)_3$ [22]. Furthermore, CSP also has a unique advantage in bridging the sintering gap among ceramics, metals, and polymers. New ceramic composites such as ZnO–polytetrafluoroethylene (PTFE) [23,24], ZnO–poly-ether-ether-ketone (PEEK) [25], SiO_2–PTFE [26], V_2O_5–poly(3,4-ethylenedioxythiophene):poly(styrene sulfonate) (PEDOT:PSS) [27], $Na_2Mo_2O_7$ (NM)-poly(ether imide) (PEI)–Ag [28], and ZnO–PEI–Cu [29] have been developed, which indicates that CSP has potential for low-temperature, high-efficiency preparation of new functional ceramics and ceramic-based composites.

More recently, CSP assisted by electric and magnetic fields was proposed, which combines CSP with SPS or FS to provide more homogeneous heating and shorter sintering time [30–32]. Gonzalez-Julian *et al.* [33] studied the coarsening of ZnO particles under various temperatures and humidities using field-assisted sintering technique/spark plasma sintering (FAST/SPS) and analyzed the cold sintering mechanisms of ZnO ceramics via Kelvin probe force microscopy. Nie *et al.* [31] reported the water-assisted flash sintering of ZnO ceramics in seconds. Kermani *et al.* [34] proposed flash cold sintering (FCS) by combining flash sintering with cold sintering, obtaining high-density ZnO and Nb_2O_5 ceramics in 60–100 s. Although CSP or electric and magnetic fields assisted CSP has been successfully applied to a wide variety of ceramic materials in a single-step sintering process, it remains challenging and sometimes causes incomplete densification [35]. In many cases, CSP serves as a pre-sintering step to promote grain-to-grain contacts, followed by a post-annealing process to achieve full densification of ceramics [36,37]. This process is similar to the two-step sintering process, whereas it allows a significant reduction in the sintering temperature compared to non-CSP-treated samples [38].

In our previous work, ZnO-based varistor ceramics with simple recipes (ZnO, Bi, Co, and Mn) were successfully prepared using CSP at 300 °C; however, the nonlinear coefficient (α) reached only 33.5 [39]. To date, it is still challenging to fabricate ZnO-based varistor ceramics via CSP because of their complex chemical systems containing approximately 90–99 wt% ZnO and various dopants with concentrations ranging from parts per million (ppm) to several percentages. In this work, multidoped ZnO-based varistor ceramics were fabricated via hybrid cold sintering process/spark plasma sintering (CSP–SPS) and post-annealing process. Typically, the CSP–SPS sample annealed at 775 °C presents the ultrahigh V_g of 1832.71 V/mm, an α value of 106.69, and an exceptionally low leakage current density (J_L) below 0.2 μA/cm^2. The effects of the microstructure and Schottky barrier at the grain boundaries on the ultrahigh voltage gradient of ZnO-based varistor ceramics are discussed.

2 Experimental

2.1 Sample preparation

ZnO powder (99.95%) with a particle size of ~206 nm was obtained from Acros Organics, USA. Bi_2O_3 (99.9%, 80–200 nm) and CoO (95%) were purchased from Alfa Aesar (Alfa Aesar Chemical Reagent Co., Ltd., Shanghai, China). Mn_2O_3 (98%), Cr_2O_3 (99.95%), Y_2O_3 (99.99%, 50 nm), In_2O_3 (99.99%, < 100 nm), NiO (99.5%, < 30 nm), CaO (98%, < 160 nm), and acetic acid (99.8%) were purchased from Aladdin (Bio-Chem Technology Co., Ltd., China). ZnO powder (93.4875 mol%) and other dopants, such as Bi_2O_3 (1.2 mol%), CoO (2.2 mol%), Mn_2O_3 (0.25 mol%), NiO (1.3 mol%), Cr_2O_3 (0.1 mol%), CaO (1.0 mol%), Y_2O_3 (0.45 mol%), and In_2O_3 (0.0125 mol%) were mixed with ethanol by ball milling at a rotating speed of 380 r/min for 12 h. Afterwards, the mixture was dried in an air circulation oven at 80 °C for 12 h.

Densification of ZnO-based varistor ceramics was carried out using the CSP–SPS route using a SPS equipment (211Lx, Fuji Electronic Industrial Co., Ltd., Japan). A 20 wt% acetic acid aqueous solution (2 mol/L) was added to the mixed powder as the liquid phase, and then, the moist powder was homogeneously ground using a high shear process with a mortar and pestle. Afterwards, the mixture was transferred into a graphite die (10.5 mm in diameter) and uniaxially pressed under 50 MPa. The die was heated to the target sintering temperature (200–300 °C) with a ramp rate of 50 °C/min under vacuum (0.1 mbar), followed by isothermal holding at the target temperature for 5–20 min. Finally, the sample was taken out from the die after the furnace cooled to room temperature. The detailed CSP–SPS process of the samples is shown in Fig. S1 in the Electronic Supplementary Material (ESM). The samples prepared under different CSP–SPS conditions are denoted as S-temperature-time. For example, for S-200-5, the sintering temperature and soaking time are 200 °C and 5 min, respectively. Moreover, pure ZnO ceramics (denoted as CSP–SPS-300) were also prepared by CSP–SPS at 300 °C for comparison. Considering that CSP–SPS is carried out in a low-oxygen partial pressure environment, the samples require further heat treatment in air to regulate grain boundary defects, thereby improving their electrical properties. The sample S-300-10 was selected for annealing at 700–900 °C for 1 h and then cooled with furnace. The detailed annealing process is also illustrated in Fig. S1 in the ESM. The samples S-300-10 annealed at different temperatures are denoted as S-A-tem. (tem., annealing temperature).

2.2 Characterizations

The densities of the samples were measured by the mass/geometry ratio and the Archimedes method with ethanol as the liquid medium. The crystal structures of the powders and ceramic samples were determined via an X-ray diffractometer (XRD; Empyrean, PANalytical, Netherlands) with Cu Kα radiation. The diffraction data were collected from 10° to 90° at a step size of 0.026°. Microstructural observations were carried out on the cross-sections of the samples using a field-emission scanning electron microscope (SEM; JSM-6390A, JEOL, Japan). A transmission electron microscope (TEM; FEI Talos F200X, USA) equipped with energy dispersive spectroscopy (EDS) were used to observe the microstructures and compositions of the grain boundaries (GBs). The valence states of the ZnO-based varistor ceramics before and after annealing were tested by an X-ray photoelectron spectrometer (XPS; K-Alpha, Thermo Scientific, USA). The X-ray source was produced at a power of 72 W (12 kV, 6 mA), and the analysis chamber was equipped with a vacuum below 2.0×10^{-7} mbar. The binding energy scale was calibrated with the C 1s line (284.8 eV) from the adventitious carbon contamination layer to ensure accurate measurement of the chemical states.

The ceramic samples were polished with sandpaper, and the final size was 1 mm in thickness and 10 mm in diameter. Au electrodes with a diameter of 5 mm were sputtered on both sides

of the samples by a high-resolution sputtering coater (Q150TS, Quorum, UK). The current density–electric field (J–E) characteristics were measured using a precise high-voltage digital sourcemeter (R2-P60W300, Dalian Haifu Technology Co., Ltd., China), a picoammeter (DMM6500, Keithley, USA), and a delta oven (Delta 9023, Delta Design, USA) from room temperature to 120 °C. The voltage gradient was obtained through $V_g = U_{1\ mA}/d$, and the nonlinear coefficient was calculated with $\alpha = 1/\log(U_{1\ mA}/U_{0.1\ mA})$, where d is the thickness of the sample, and $U_{1\ mA}$ and $U_{0.1\ mA}$ are the voltages at current densities of 1 and 0.1 mA/cm^2, respectively. The impedance spectra were obtained via a broadband dielectric spectrometer (Concept 80, Novocontrol, Germany) in the frequency range from 0.1 Hz to 1 MHz over the temperature range of 25–200 °C, using 1 V alternating current (AC) signals for excitation.

3 Results and discussion

The densification behavior of ZnO-based varistor ceramics was investigated by monitoring the displacement of punch rods induced by powder shrinkage during CSP–SPS. The shrinkage (η) of a sample can be calculated by Eq. (1):

$$\eta = \frac{L_0 - L_T}{L_0} \times 100\% \quad (1)$$

where L_0 is the initial thickness of the samples at room temperature under an external pressure of 50 MPa, and L_T is the thickness of the sample at the sintering temperature of T. Figure 1(a) shows that the densification process of ZnO-based varistor ceramics during CSP–SPS can be divided into three different stages. In the first stage (from room temperature to ~105 °C), the sample exhibits a relatively small shrinkage of 3.38%. In the second stage (105–200 °C), a significant shrinkage of 28.04% can be observed. As the sintering temperature increases to the third stage (200–300 °C), the shrinkage decreases to 4.60%. The three shrinking stages of ZnO-based varistor ceramics can be attributed to particle dissolution–rearrangement, rearrangement–dissolution–precipitation, and grain growth during CSP–SPS [40]. Notably, the rapid densification starts at 105 °C for S-300-10, which is relatively delayed compared with pure ZnO ceramics occurring at 87 °C, as shown in Fig. 1(a) and Fig. S2(a) in the ESM. The mass transfer and grain growth in S-300-10 may be hindered by the doped metal oxides [41], which affects the densification process during CSP–SPS process. The densification mechanisms can be described by the Kingery liquid-phase sintering model [42], and the shrinkage dependence given by Eq. (2) determines the change of linear shrinkage.

$$\frac{L_0 - L_t}{L_0} = Kt^n \quad (2)$$

where L_0 is the initial thickness of the sample; L_t is the thickness of the sample at the sintering time of t; K is a constant related to the material and sintering conditions. The densification rates at each stage can be determined by n in Eq. (2). When n is equal to 2 or 3, it indicates that reaction or diffusion is the dominant mechanism during the formation of spherical or equiaxed particles, while for angular particles, n is equal to 3 or 5 at the same stage. Figure 1(b) shows that the slope of S-300-10 in the second stage is 2.69, which is greater than the reported slope of 1 for the conventional liquid-phase sintering method but less than the slope of 3.13 for the pure ZnO ceramics sintered by CSP–SPS (Fig. S2(b) in the ESM). Therefore, it is believed that the pressure and electric field applied

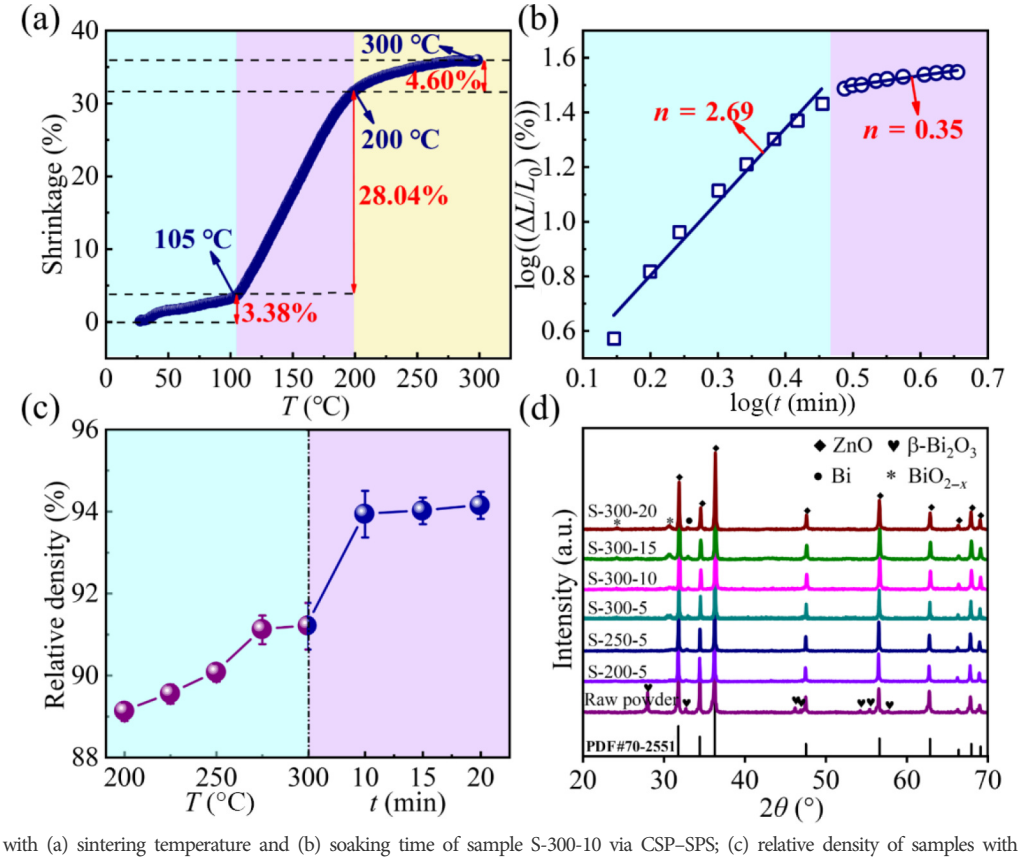

Fig. 1 Shrinkage with (a) sintering temperature and (b) soaking time of sample S-300-10 via CSP–SPS; (c) relative density of samples with different sintering temperatures and soaking time. (d) XRD patterns of mixed powder and ZnO-based varistor ceramics prepared using CSP–SPS at different sintering temperatures and soaking time.

in CSP–SPS may greatly promote mass transfer during sintering. The pressure is beneficial for enhancing the contact between particles and reducing the diffusion distance, whereas the electric field is helpful for accelerating the migration of charged species and facilitating the mass transfer process [43,44]. However, the inconsistent dissolution of various dopants in acetic acid solution may block the densification process. Non-uniform dissolution during CSP leads to an inhomogeneous distribution of dopants, which disrupts the regular mass-transfer paths and restrains the formation of a continuous densification network [17]. During the third stage, both pure ZnO ceramics and the doped sample S-300-10 show shrinkage slopes of approximately 1/3, which is consistent with the phase-boundary controlled case in Kingery's model [40,45]. Generally, in the phase boundary-controlled sintering process, the densification rate is limited by the movement of solid–liquid phase boundaries. As the solid particles dissolve into the liquid phase and precipitate at the contact points, the phase boundaries gradually move and drive the shrinkage of the sample.

Figure 1(c) shows the relative density of ZnO-based varistor ceramics as functions of sintering temperature and time. Samples sintered at 200 °C for 5 min show approximately 89.1% relative density, while the value increases to ~91.2% when sintered at 300 °C for 5 min. Furthermore, the relative density of the samples is further increased to ~94% by extending the soaking time to 10 min. However, the relative density of ZnO-based varistor ceramics does not clearly increase with increasing soaking time up to 20 min, which is much lower than the 99.1% of the pure ZnO ceramic fabricated via CSP–SPS, as shown in Fig. S2(c) in the ESM. Thus, the densification of ZnO-based varistor ceramics is not well completed because of the incongruent dissolution of ZnO and doped oxides in acetic acid solution during CSP–SPS [35].

Figure 1(d) shows the XRD patterns of the mixed powder and ZnO-based varistor ceramics prepared under different CSP–SPS conditions. ZnO with a hexagonal wurtzite crystal structure (PDF#70-2551) and β-Bi_2O_3 were observed in the powder mixture, while other dopants were not detected, probably because of their low content. In the ZnO-based varistor ceramics, BiO_{2-x} and Bi are found, and their diffraction peaks increase with increasing sintering time at 300 °C. It is demonstrated that Bi_2O_3 is reduced into Bi and BiO_{2-x} because the CSP–SPS process occurs under an atmosphere of low oxygen partial pressure, and an increase in sintering temperature and soaking time further promotes the reduction reaction [10,46].

Figures 2(a)–2(c) show the microstructures of ZnO-based varistor ceramics under different CSP–SPS conditions. The grain size of each sample was measured using the Nano measurer software, and the average grain size (l) was evaluated via the line intercept method [47], as shown in the insets of Figs. 2(a)–2(c). The ZnO-based varistor ceramics exhibit dense microstructures with grain size increasing slightly as the sintering temperature and soaking time increase. The grain size of S-300-10 is ~253 nm, which is larger than that of the starting ZnO powder (~206 nm, shown in Fig. S3(a) in the ESM), indicating that ZnO-based varistor ceramics experience a typical sintering process. However, the value is substantially smaller than that of the pure ZnO ceramics (~615 nm) prepared with the same CSP–SPS conditions, as shown in Fig. S3(b) in the ESM. Moreover, some small needle-like or flaky particles are also observed in Figs. 2(a)–2(c), which may be the precipitates of doped Bi_2O_3, Y_2O_3, etc., generated during the CSP–SPS process, and a similar phenomenon has also been reported in cold-sintered yttria-stabilized bismuth oxide ceramics [48]. More details of the small particles were also determined via TEM. As shown in Figs. 2(d)–2(f), the majority of the ZnO particles have significantly grown and evolved into polygonal grains, and many small uncoarsened round nanoparticles and needle-like precipitates were observed between the ZnO grains, which were also proven to be dopants through the EDS map, as shown in Fig. 2(g). The details of the distribution of each dopant are shown in Fig. S4 in the ESM.

The V_g and α are important electrical indicators of ZnO-based varistor ceramics. The J–E characteristic curves of the CSP–SPS samples are shown in Fig. 3(a), and the electric parameters, such as V_g and α, are displayed in Table 1. The J–E curves of the CSP–SPS samples have nearly linear ohmic characteristics, with very low V_g values ranging from 0.42 to 6.01 V/mm, α value of only ~1, and leakage current densities as high as 723–831 μA/cm^2. The transient liquid phase used during CSP–SPS of ZnO varistor ceramics promotes mass transfer via a dissolution–precipitation process. However, the amorphous phases at the grain boundaries cannot transform into crystalline phases or spinels under the low temperature conditions of CSP–SPS [18]. Additionally, the metal Bi and oxygen vacancies resulting from the vacuum condition (0.1 mbar) of CSP–SPS may lead to the failure of the double

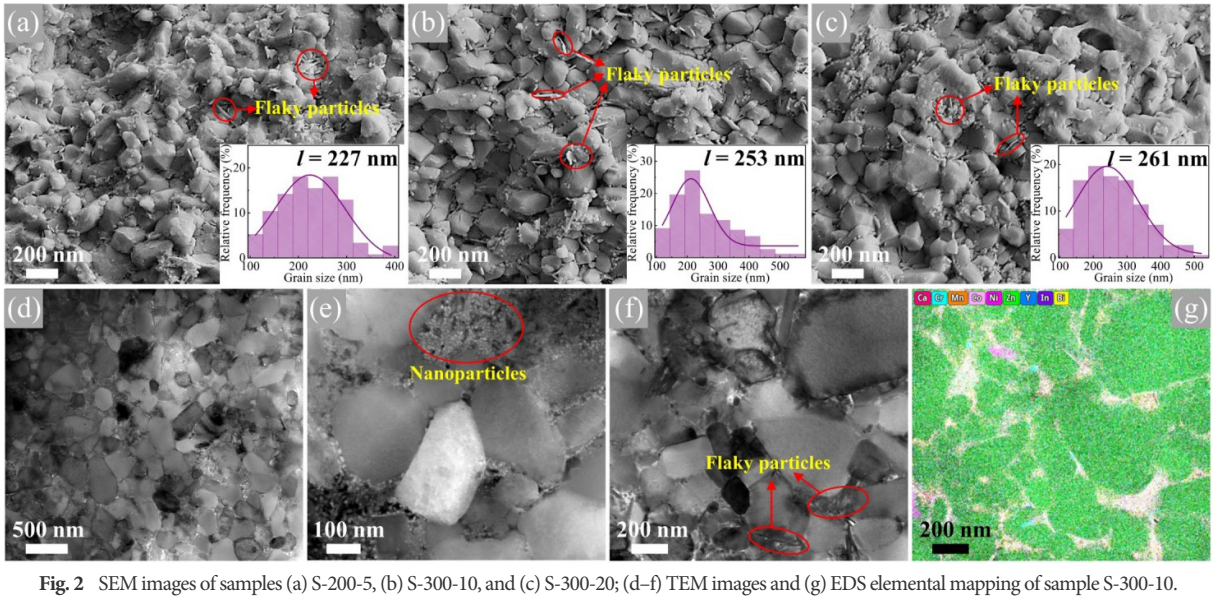

Fig. 2 SEM images of samples (a) S-200-5, (b) S-300-10, and (c) S-300-20; (d–f) TEM images and (g) EDS elemental mapping of sample S-300-10.

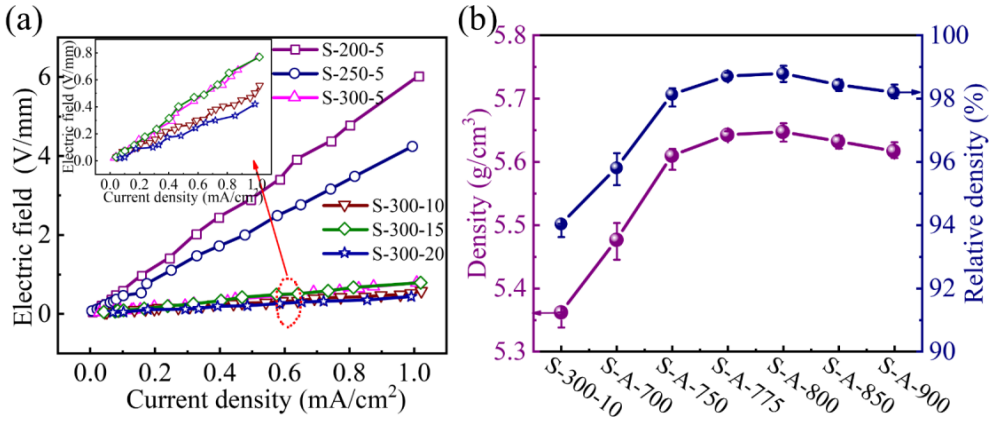

Fig. 3 (a) *J*–*E* characteristics of ZnO varistor ceramic samples sintered at different temperatures and soaking time. (b) Density of ZnO varistor ceramics at different annealing temperatures.

Table 1 Parameters of ZnO ceramic samples sintered at different temperatures and soaking time

Sample	V_g (V/mm)	α	J_L (μA/cm²)	l (nm)
S-200-5	6.01	0.99	744.69	227
S-250-5	4.23	1.02	744.85	240
S-300-5	0.77	0.97	831.90	245
S-300-10	0.56	1.16	829.43	253
S-300-15	0.77	0.95	737.37	256
S-300-20	0.42	0.94	723.36	261

Schottky barriers at the grain boundaries, and thus the samples do not present nonlinear *J*–*E* behavior. Therefore, post-annealing is required to enhance densification and improve electrical properties. The densities of the ZnO varistor ceramics annealed at different temperatures are shown in Fig. 3(b). The relative density of sample S-300-10 is enhanced with increasing annealing temperature, reaching a maximum value of 98.79% at 800 °C. However, as the annealing temperature is further increased to 900 °C, volatilization of the Bi_2O_3 dopant may occur, leading to a slight decrease in the density of ZnO varistor ceramics [49].

The micromorphology of the annealed samples is shown in Figs. 4(a)–4(f), and the grain size distributions are shown in the insets. The needle-like or flaky precipitates observed in the CSP–SPS samples clearly disappear after the annealing process. The ZnO grain size clearly increases from 253 nm for sample S-300-10 (Fig. 2(b)) to 0.38 μm for sample S-A-700 after annealing at 700 °C. When the annealing temperature increases to 750 °C

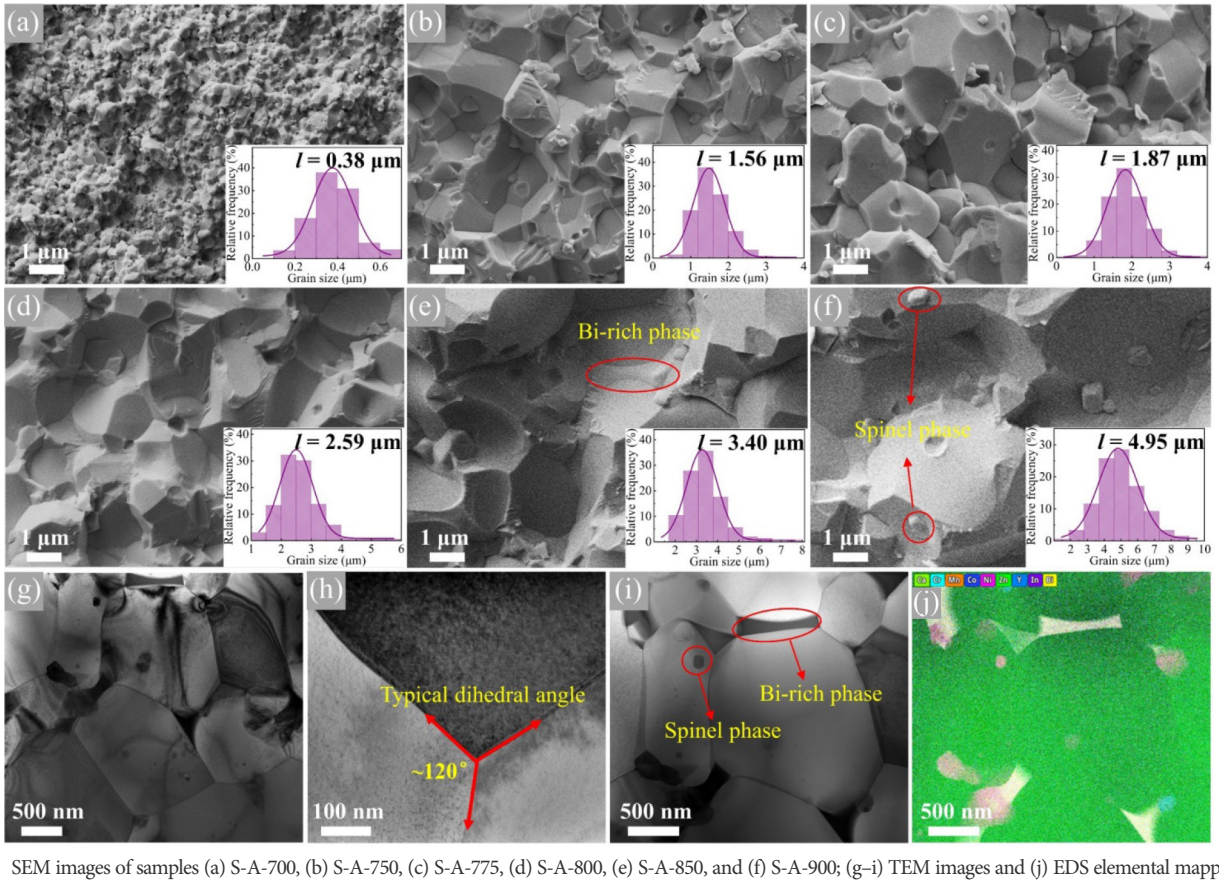

Fig. 4 SEM images of samples (a) S-A-700, (b) S-A-750, (c) S-A-775, (d) S-A-800, (e) S-A-850, and (f) S-A-900; (g–i) TEM images and (j) EDS elemental mapping of sample S-A-775.

and above, the grains grow sharply, and the microstructure becomes more tightly packed. Although the ZnO grain size gradually increases to 4.95 μm after 900 °C annealing, it is still much smaller than the grain size of commercial ZnO-based varistor ceramics (> 10 μm) [49]. These findings indicate that ZnO-based varistor ceramics with smaller and more uniform grains can be obtained via CSP–SPS and low-temperature annealing.

As shown in Figs. 4(g)–4(j), the microstructure and elemental distribution of sample S-A-775 were further analyzed using TEM and EDS. Figures 4(g) and 4(h) show a typical dense granular microstructure with no indication of porosity. An equilibrated dihedral angle of 120° at triple points and ordered grain arrangements can be observed, suggesting that the sample achieves a specific microstructural steady state. This state is beneficial for minimizing electron scattering at grain boundaries and enhancing electrical properties [50]. As shown in Fig. 4(i) and 4(j), the Bi-rich phase is distributed at the grain boundaries and triple junction points, which is related to the tetragonal β-Bi_2O_3 phase based on the selected area electron diffraction (SAED) along the [110] zone axis in Fig. S5 in the ESM. More details of the element distribution in sample S-A-775 can be found in Fig. S6 in the ESM. In addition, Fig. S7 and Tables S1–S3 in the ESM present the element ratios from the ZnO grain boundaries, grains and spinels determined via EDS. The results show that Y, Ca, and Cr are predominantly located at the grain boundaries and triple junction points. It is believed that dopants such as Y_2O_3, CaO, and Cr_2O_3 may react with Bi_2O_3 to generate new compounds (e.g., Bi_3YO_6, $Bi_6Ca_4O_{13}$, and $CrBi_{18}O_{30}$), which play crucial roles in inhibiting Bi_2O_3 evaporation and enhancing the electrical performance of ZnO varistors [51]. Moreover, Mn, Ni, Co, Zn, and O can be detected on the small spinel embedded in the ZnO grains. Therefore, CoO, Mn_2O_3, and NiO may react with ZnO to produce spinel phases with AB_2O_4 chemical structures during the annealing process.

XPS analysis was used to detect O element and its chemical valence state in the ZnO varistor samples before and after annealing. The XPS spectra of O elements in samples S-300-10 and S-A-775 are shown in Fig. 5(a) and 5(b). The collected data were analyzed via XPSPEAK software, and Shirley-type background subtraction was used to fit the curves [52]. The relative contents of O element were calculated through deconvolution of the XPS peaks, as shown in Fig. 5(c). The deconvoluted O 1s spectrum contained two peaks of O_L (~529.8 eV) and O_C (~531.6 eV), which are related to lattice oxygen and adsorbed oxygen, respectively [53]. Figure 5(c) shows significant differences between the relative amounts of O_L and O_C in samples S-300-10 and S-A-775. After annealing at 775 °C, the percentage of O_C notably increases from 25.46% for sample S-300-10 to 48.54% for sample S-A-775, which indicates that annealing in an air atmosphere promotes the diffusion of oxygen (O_2(g)) towards the grain boundaries. At these boundaries, oxygen captures free electrons, thereby resulting in a higher O_C concentration [53]. Moreover, O_C can capture electrons, establishing a negatively charged interfacial layer, and elevating the grain boundary potential barrier [54], thus improving the nonlinear *J*–*E* characteristics. Since ZnO varistor ceramics prepared under low oxygen partial pressure are susceptible to oxygen vacancy defects, post-annealing is generally required to promote the migration of oxygen atoms and optimize the lattice structure [53,54].

Figure 6(a) shows the XRD patterns of ZnO-based varistor ceramics prepared with CSP–SPS and the annealing process. The metal Bi phase and BiO_{2-x} phase disappear after annealing, while the Bi-rich phases appear. The above phenomena are consistent with the results of TEM and EDS analyses. Typically, CaO and Y_2O_3 undergo a solid-solution reaction with Bi_2O_3 to produce Bi_3YO_6 and $Bi_6Ca_4O_{13}$ during the annealing process, which are important in building the Schottky barrier between ZnO grains and inducing the nonlinear ohmic properties of ZnO varistor ceramics. Moreover, the magnified view of XRD patterns in Fig. 6(a) shows that the diffraction intensity of the Bi-rich phase increases with increasing annealing temperature from 700 to 775 °C, while the diffraction intensity is slightly reduced as the annealing temperature further increases to 800–900 °C, which can be attributed to the volatilization of the Bi-rich phase at high temperatures [49]. The *J*–*E* characteristics of the annealed ZnO-based varistor ceramics were measured at room temperature, as shown in Figs. 6(b), 6(c), and Table 2. The V_g of sample S-A-700 sharply increases to 10,210.01 V/mm after annealing at 700 °C, while the nonlinear coefficient is only 15.53. The high V_g is closely related to its fine grain size, as shown in Fig. 4(a). After annealing, the grain size of CSP–SPS samples is still less than 4.95 μm, which is much smaller than that of conventionally sintered samples (> 10 μm) [49]. However, the low annealing temperature of 700 °C could not promote the Bi-rich phase to produce high-resistance grain boundaries between the ZnO grains, giving rise to low α [55]. Generally, a nonlinear coefficient below 40 remains inadequate to meet industrial demands [49]. As the annealing temperature rises to 775 °C, α reaches a maximum of 106.96, and V_g remains at 1832.71 V/mm, which is approximately 3.7–9.2 times greater than that of current state-of-the-art commercial varistor ceramics (V_g = 200–500 V/mm, α < 60) [49]. However, when the annealing temperature exceeds 825 °C, volatilization of the Bi-rich phase may lead to a decrease in α. Figure 6(d) compares V_g and α of ZnO-based varistor ceramics prepared using different sintering techniques [10–14,49,49,53,55–61]. The strategy using CSP–SPS with post-annealing clearly has advantages in reducing the sintering temperature and improving

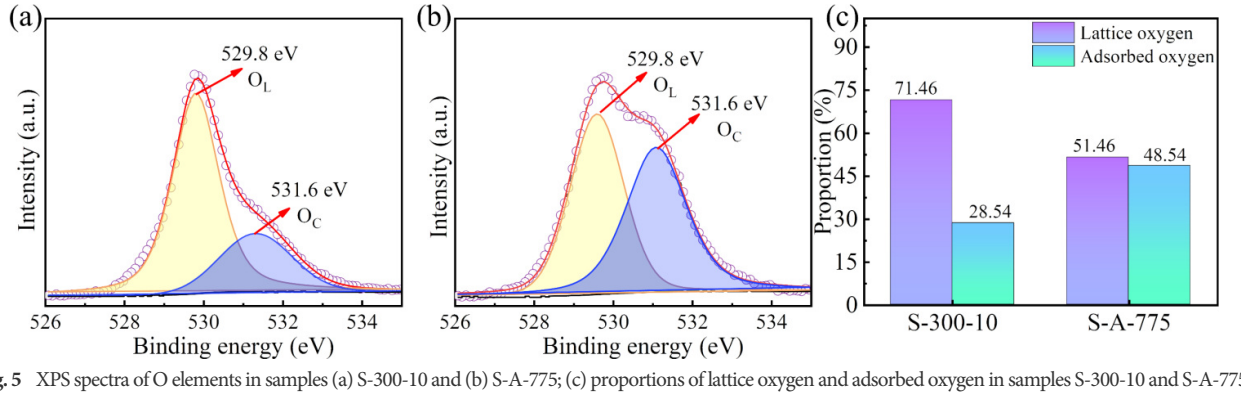

Fig. 5 XPS spectra of O elements in samples (a) S-300-10 and (b) S-A-775; (c) proportions of lattice oxygen and adsorbed oxygen in samples S-300-10 and S-A-775.

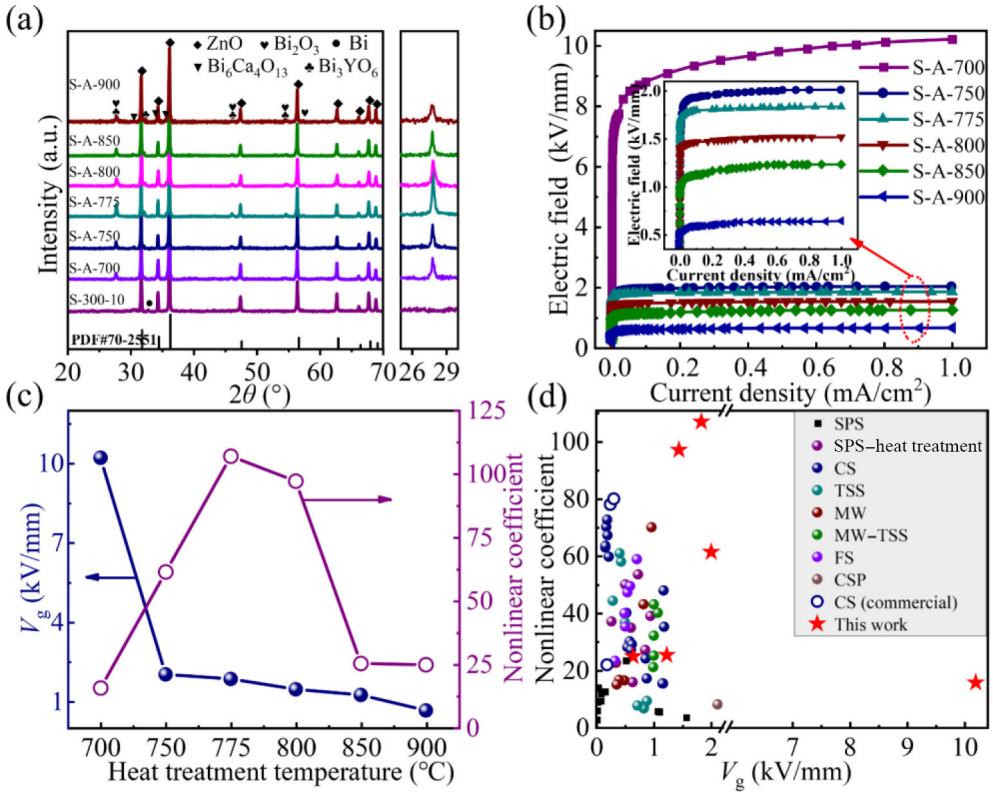

Fig. 6 (a) XRD patterns and (b) nonlinear *J*–*E* characteristics of ZnO varistor ceramics at different annealing temperatures. (c) Overall summary of V_g and α. (d) Comparison of V_g vs. α of ZnO varistor ceramics with various sintering techniques (CS: conventional sintering, TSS: two-step sintering).

Table 2 Parameters of ZnO varistor ceramics at different annealing temperatures

Sample	V_g (V/mm)	α	J_L (μA/cm²)	l (μm)
S-A-700	10210.01	15.53	~11.70	0.38
S-A-750	2005.15	61.33	~0.26	1.56
S-A-775	1832.71	106.96	< 0.20	1.87
S-A-800	1441.44	97.13	< 0.20	2.59
S-A-850	1228.87	25.18	~7.80	3.40
S-A-900	639.29	24.70	~9.20	4.95

the nonlinear *J*–*E* characteristics of the ZnO-based varistor ceramics.

The Schottky thermionic emission current can be described as Eq. (3) [62]:

$$J = A^* T^2 \exp\left(\frac{\beta\sqrt{E} - q\varphi_B}{kT}\right) \quad (3)$$

where J is the current density (mA/cm²); A^* is the Richardson constant; T is the absolute temperature (K); β is a constant; E is the applied electric field (V/cm); q is the charge (C); k is the Boltzmann constant; φ_B is the Schottky barrier height (eV). $\ln(J/T^2)$ and $E^{1/2}$ have a linear relationship at low electric fields, as shown in Figs. 7(a)–7(f), indicating that Schottky emission dominates the conduction mechanism at the grain boundary barriers of the samples annealed under low electric fields. The insets of Figs. 7(a)–7(f) illustrate the barrier heights calculated via Arrhenius fitting ($1/T$ vs. $\ln(J/T^2)$). Figure 7(g) shows the variation curves of φ_B at different annealing temperatures. At low annealing temperatures of 700–750 °C, the temperature is not high enough to produce the liquid Bi-rich phase and promote the densification of the ZnO varistor ceramics, as shown in Fig. 3(b). Moreover, a low annealing temperature cannot drive the diffusion and reaction of various dopants at the grain boundaries, resulting in a low Schottky barrier in ZnO varistor ceramics [10]. When annealed at 775 °C, the highly dense sample presents a high Schottky barrier of 1.01 eV. This means that a large grain boundary resistance is achieved, which enables a high voltage gradient, non-linear coefficient, and low leakage current density. However, if the annealing temperature is too high, the Bi-rich phase may volatilize and destroy the high-resistance grain boundary structure, lowering the Schottky barrier height and deteriorating the electrical properties [49]. Under high electric fields, electrons can tunnel through the potential barriers at the grain boundaries, and the tunneling current follows the Fowler–Nordheim equation as Eq. (4) [63]:

$$J = A^* E^2 \exp\left(\frac{-\gamma}{E}\right) \quad (4)$$

where γ is a constant. Figure 7(h) shows the Fowler–Nordheim plot for sample S-A-775. The linear relationship between $\ln(J/E^2)$ and $1/E$ confirms electron tunneling as the dominant conduction mechanism of S-A-775 under high electric fields. Thus, both Schottky emission and electron tunneling control the electric conduction of ZnO-based varistor ceramics at low and high electrical fields, respectively, as illustrated in Fig. 7(i).

The temperature-dependent impedance spectra of samples S-300-10 and S-A-775 are shown in Figs. 8(a) and 8(b). As the temperature increases from 140 to 180 °C, the intercepts at the low frequency limit of the semicircles shift toward lower Z' regions, revealing that the resistance of grain boundaries decreases with increasing temperature. Moreover, the grain boundary resistance (R_{gb}) of sample S-A-775 is approximately five orders of magnitude higher than that of sample S-300-10 at the sample temperature, which can be attributed mainly to the optimization

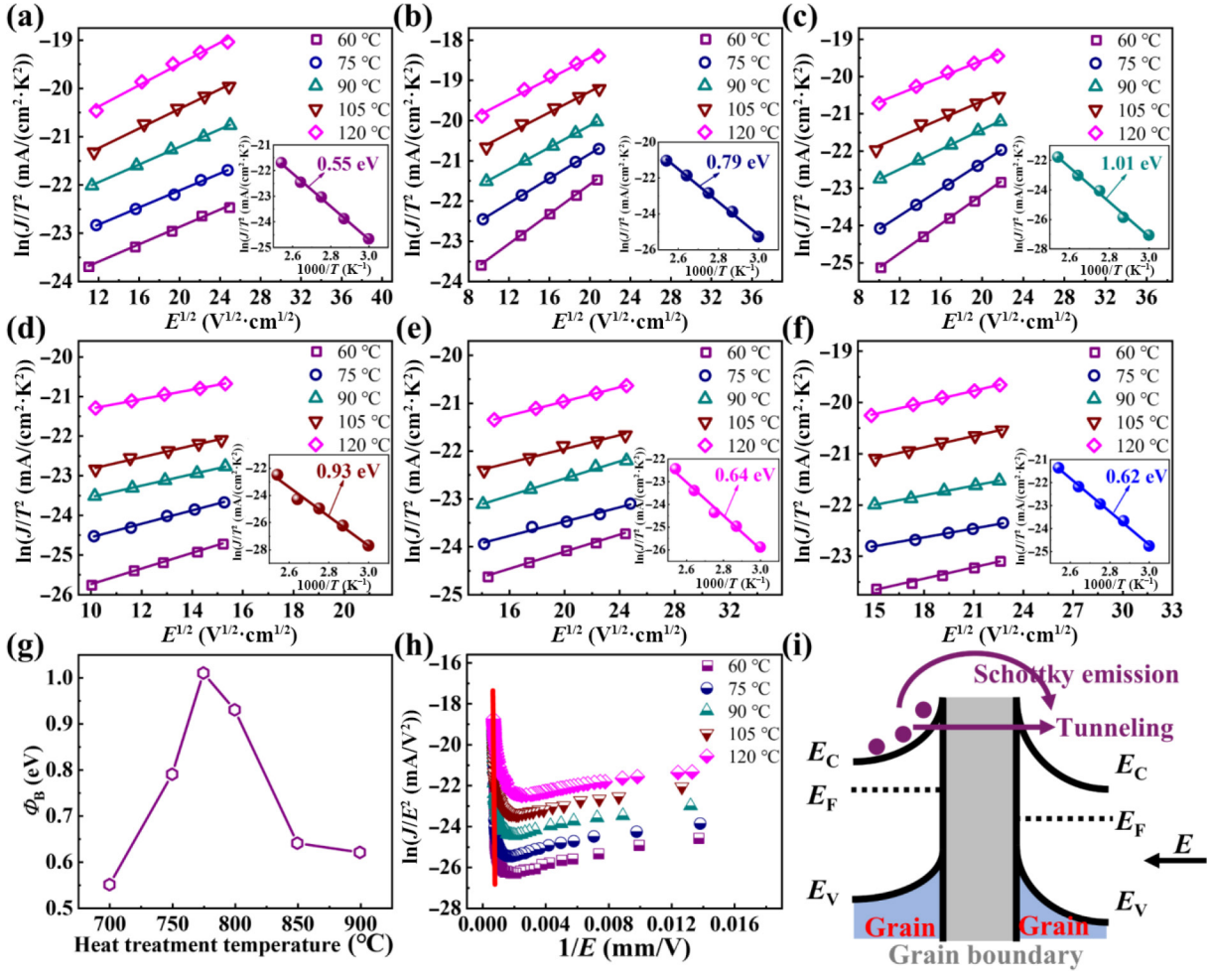

Fig. 7 ln(J/T^2) versus $E^{1/2}$ and ln(J/T^2) versus 1/T plots for samples (a) S-A-700, (b) S-A-750, (c) S-A-775, (d) S-A-800, (e) S-A-850, and (f) S-A-900. (g) Overall summary of the Schottky barrier height. (h) Fowler–Nordheim plot of sample S-A-775. (i) Schematic diagram of the possible conductive mechanism of annealed ZnO-based varistor samples (E_C is the conduction band; E_F is the Fermi level; E_V is the valence band).

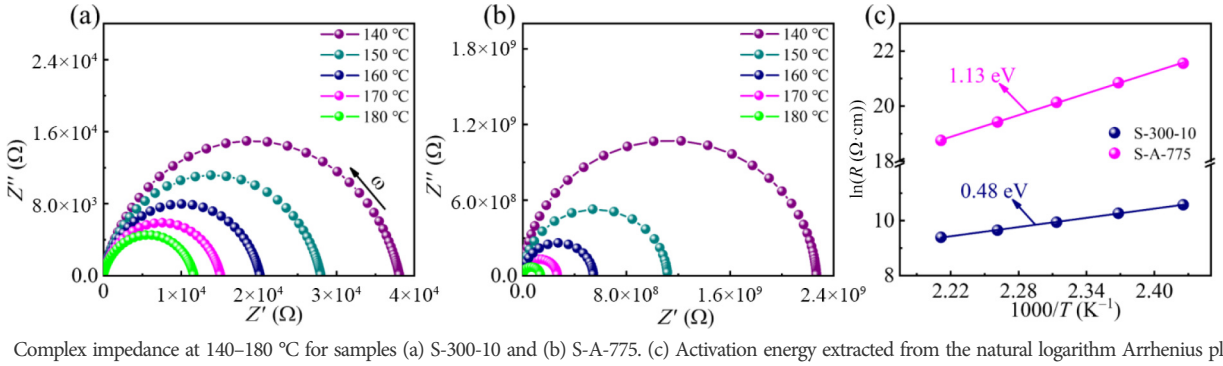

Fig. 8 Complex impedance at 140–180 °C for samples (a) S-300-10 and (b) S-A-775. (c) Activation energy extracted from the natural logarithm Arrhenius plot for samples S-300-10 and S-A-775.

of grain boundary phases and the regulation of defect structures during the post-annealing process [53]. The grain boundary resistance follows the temperature-dependent Arrhenius relationship, as Eq. (5) [64]:

$$R_{gb} = R_0 \exp\left(\frac{E_A}{kT}\right) \quad (5)$$

where R_0 is a constant; E_A is the activation energy (eV); k is the Boltzmann constant; T is the absolute temperature (K). R_{gb}, extracted from the Z'–Z'' plots, was analyzed using Eq. (5), and the activation energy was calculated from the slope of lnR_{gb} versus 1/T. As shown in Fig. 8(c), the activation energy is significantly increased from 0.48 eV for sample S-300-10 to 1.13 eV for sample S-A-775 after annealing at 775 °C, which may be influenced primarily by O_C defects near the grain boundaries [53]. A higher E_A implies greater difficulty in carrier (e.g., electron) migration, particularly when the leakage current flowing over the grain boundaries is restricted.

4 Conclusions

In summary, ultrahigh voltage-gradient ZnO-based varistor ceramics were prepared through novel CSP–SPS and post-

annealing process. ZnO-based varistor ceramics were initially densified through CSP–SPS at 300 °C and then annealed at 700–900 °C in an air atmosphere. It is found that the relative density of the ZnO-based varistor ceramic reaches ~98.79%, with a micron grain size of 1.87 μm after annealing at 775 °C. Furthermore, post-annealing provides sufficient energy for phase transformation and formation of high-resistance grain boundaries, thereby realizing the ultrahigh V_g of ~1832.71 V/mm and an excellent nonlinear coefficient of ~106.96. A high grain-boundary activation energy of 1.13 eV effectively limits the leakage current of the annealed samples. This work provides a potential route to produce high-performance ZnO-based varistor ceramics via CSP–SPS and low-temperature annealing process.

Acknowledgements

This work was supported by the Joint Funds of the National Natural Science Foundation of China (No. U23B20115) and the Fok Ying-Tong Education Foundation, China (No. 171050). The authors extend their gratitude to the Sinoma Institute of Materials Research (Guangzhou, China) Co., Ltd., for the TEM tests and Mr. Dazhong Wan from the Shiyanjia Laboratory (www.shiyanjia.com) for assisting with the XPS analysis.

Availability of data and materials

The data that support the findings of this study are available from the corresponding author upon reasonable request.

Competing interests

The authors have no competing interests to declare that are relevant to the content of this article.

Electronic Supplementary Material

Supplementary material is available in the online version of this article at https://doi.org/10.26599/JAC.2025.9221065.

References

[1] Li ST, Li JY, Liu WF, *et al.* Advances in ZnO varistors in China during the past 30 years-fundamentals, processing, and applications. *IEEE Electr Insul Mag* 2015, **31**: 35–44.

[2] Greuter F. ZnO varistors: From grain boundaries to power applications. In: *Oxide Electronics*. Ray A, Ed. Chichester: John Wiley & Sons, 2021: 157–234.

[3] Liu ZH, Zhang FX, Yu J, *et al.* Research on key technologies in ±1100 kV ultra-high voltage DC transmission. *High Volt* 2018, **3**: 279–288.

[4] Jiang F, Peng ZJ, Zang YX, *et al.* Progress on rare-earth doped ZnO-based varistor materials. *J Adv Ceram* 2013, **2**: 201–212.

[5] Meng PF, Hu J, Wu J, *et al.* Comprehensive performances of ZnO varistors tailored by multielements doping. *High Volt Eng* 2018, **44:** 241–247. (in Chinese)

[6] Liu WF, Zhang L, Kong FY, *et al.* Enhanced voltage gradient and energy absorption capability in ZnO varistor ceramics by using nano-sized ZnO powders. *J Alloys Compd* 2020, **828**: 154252.

[7] Van Beneden B. Varistors: Ideal solution to surge protection. *Power Electron Technol* 2003, **29**: 26–34.

[8] He JL. *Metal Oxide Varistors: From Microstructure to Macro-characteristics*. Hoboken (USA): John Wiley & Sons, 2019.

[9] Beynet Y, Izoulet A, Guillemet-Fritsch S, *et al.* ZnO-based varistors prepared by spark plasma sintering. *J Eur Ceram Soc* 2015, **35**: 1199–1208.

[10] Macary LS, Kahn ML, Estournès C, *et al.* Size effect on properties of varistors made from zinc oxide nano-particles through low temperature spark plasma sintering. *Adv Funct Mater* 2009, **19**: 1775–1783.

[11] Gunnewiek RFK, Kiminami RHGA. Two-step microwave sintering of nanostructured ZnO-based varistors. *Ceram Int* 2017, **43**: 847–853.

[12] Egorov SV, Eremeev AG, Kholoptsev VV, *et al.* Rapid microwave sintering of zinc oxide-based varistor ceramics. *J Eur Ceram Soc* 2021, **41**: 6508–6515.

[13] Peng P, Deng YJ, Niu JP, *et al.* Fabrication and electrical characteristics of flash-sintered SiO_2-doped ZnO–Bi_2O_3–MnO_2 varistors. *J Adv Ceram* 2020, **9**: 683–692.

[14] Wu AX, Zhu ZX, Wang XL, *et al.* High-performance ZnO varistor ceramics prepared by arc-induced flash sintering with low energy consumption at room temperature. *High Volt* 2022, **7**: 222–232.

[15] Wang CW, Ping WW, Bai Q, *et al.* A general method to synthesize and sinter bulk ceramics in seconds. *Science* 2020, **368**: 521–526.

[16] Guo J, Floyd R, Lowum S, *et al.* Cold sintering: Progress, challenges, and future opportunities. *Annu Rev Mater Res* 2019, **49**: 275–295.

[17] Guo J, Guo HZ, Baker AL, *et al.* Cold sintering: A paradigm shift for processing and integration of ceramics. *Angew Chem Int Ed* 2016, **128**: 11629–11633.

[18] Ding JX, Guo J, Yan RJ, *et al.* Cold sintering process: A green route to fabricate thermoelectrics. *J Adv Ceram* 2024, **13**: 1697–1712.

[19] Funahashi S, Guo J, Guo HZ, *et al.* Demonstration of the cold sintering process study for the densification and grain growth of ZnO ceramics. *J Am Ceram Soc* 2017, **100**: 546–553.

[20] Tsuji K, Ndayishimiye A, Lowum S, *et al.* Single step densification of high permittivity $BaTiO_3$ ceramics at 300 °C. *J Eur Ceram Soc* 2020, **40**: 1280–1284.

[21] Kang SL, Zhao XT, Guo J, *et al.* Evolution from transparent SiO_2 glass to ceramics enabled by cold sintering with a transient chemistry: H_2SiO_3. *Scripta Mater* 2023, **233**: 115522.

[22] Berbano SS, Guo J, Guo HZ, *et al.* Cold sintering process of $Li_{1.5}Al_{0.5}Ge_{1.5}(PO_4)_3$ solid electrolyte. *J Am Ceram Soc* 2017, **100**: 2123–2135.

[23] Zhao XT, Yang Y, Cheng L, *et al.* Cold sintering process for fabrication of a superhydrophobic ZnO–polytetrafluoroethylene (PTFE) ceramic composite. *J Adv Ceram* 2023, **12**: 1758–1766.

[24] Zhao XT, Guo J, Wang K, *et al.* Introducing a ZnO–PTFE (polymer) nanocomposite varistor via the cold sintering process. *Adv Eng Mater* 2018, **20**: 1700902.

[25] Si MM, Hao JY, Zhao ED, *et al.* Preparation of zinc oxide/poly-ether-ether-ketone (PEEK) composites via the cold sintering process. *Acta Mater* 2021, **215**: 117036.

[26] Ndayishimiye A, Tsuji K, Wang K, *et al.* Sintering mechanisms and dielectric properties of cold sintered $(1–x)SiO_2$–xPTFE composites. *J Eur Ceram Soc* 2019, **39**: 4743–4751.

[27] Guo J, Guo HZ, Heidary DSB, *et al.* Semiconducting properties of cold sintered V_2O_5 ceramics and co-sintered V_2O_5–PEDOT:PSS composites. *J Eur Ceram Soc* 2017, **37**: 1529–1534.

[28] Guo J, Pfeiffenberger N, Beese A, *et al.* Cold sintering $Na_2Mo_2O_7$ ceramic with poly(ether imide) (PEI) polymer to realize high-performance composites and integrated multilayer circuits. *ACS Appl Nano Mater* 2018, **1**: 3837–3844.

[29] Wang DW, Zhou D, Song KX, *et al.* Cold-sintered C0G multilayer ceramic capacitors. *Adv Electron Mater* 2019, **5**: 1900025.

[30] Dargatz B, Gonzalez-Julian J, Bram M, *et al.* FAST/SPS sintering of nanocrystalline zinc oxide—Part I: Enhanced densification and formation of hydrogen-related defects in presence of adsorbed water. *J Eur Ceram Soc* 2016, **36**: 1207–1220.

[31] Nie J, Zhang Y, Chan JM, *et al.* Water-assisted flash sintering: Flashing ZnO at room temperature to achieve ~98% density in seconds. *Scripta Mater* 2018, **142**: 79–82.

[32] Liang J, Zhao XT, Kang SL, *et al.* Microstructural evolution of ZnO via hybrid cold sintering/spark plasma sintering. *J Eur Ceram Soc* 2022, **42**: 5738–5746.

[33] Gonzalez-Julian J, Neuhaus K, Bernemann M, *et al.* Unveiling the mechanisms of cold sintering of ZnO at 250 °C by varying applied stress and characterizing grain boundaries by Kelvin Probe Force Microscopy. *Acta Mater* 2018, **144**: 116–128.

[34] Kermani M, Biesuz M, Dong J, *et al.* Flash cold sintering: Combining water and electricity. *J Eur Ceram Soc* 2020, **40**: 6266–6271.

[35] Ndayishimiye A, Sengul MY, Sada T, *et al.* Roadmap for densification in cold sintering: chemical pathways. *Open Ceram* 2020, **2**: 100019.
[36] Kabir A, Espineira-Cachaza M, Fiordaliso EM, *et al.* Effect of cold sintering process (CSP) on the electro–chemo–mechanical properties of Gd-doped ceria (GDC). *J Eur Ceram Soc* 2020, **40**: 5612–5618.
[37] Guo HZ, Guo J, Baker A, *et al.* Cold sintering process for ZrO_2-based ceramics: Significantly enhanced densification evolution in yttria-doped ZrO_2. *J Am Ceram Soc* 2017, **100**: 491–495.
[38] de Beauvoir TH, Taberna PL, Simon P, *et al.* Cold sintering process characterization by in operando electrochemical impedance spectroscopy. *J Eur Ceram Soc* 2022, **42**: 5747–5755.
[39] Zhao XT, Liang J, Sun JJ, *et al.* Cold sintering ZnO based varistor ceramics with controlled grain growth to realize superior breakdown electric field. *J Eur Ceram Soc* 2021, **41**: 430–435.
[40] Si MM, Li XY, Fu CL, *et al.* Cold sintering assisted processing of Mn–Zn ferrites. *J Eur Ceram Soc* 2023, **43**: 6145–6153.
[41] Galotta A, Sglavo VM. The cold sintering process: A review on processing features, densification mechanisms and perspectives. *J Eur Ceram Soc* 2021, **41**: 1–17.
[42] Kingery WD. Densification during sintering in the presence of a liquid phase. I. theory. *J Appl Phys* 1959, **30**: 301–306.
[43] German R. *Sintering: From Empirical Observations to Scientific Principles*. Oxford (UK): Elsevier, 2014.
[44] Guillon O, Rheinheimer W, Bram M. A perspective on emerging and future sintering technologies of ceramic materials. *Adv Eng Mater* 2023, **25**: 2201870.
[45] Li XM, Fu CL, Xu WC, *et al.* Hybrid low-temperature sintering processes of electro-ceramics. *J Am Ceram Soc* 2024, **107**: 1996–2009.
[46] Liang J, Zhao XT, Sun JJ, *et al.* Enhanced electrical properties of ZnO varistor ceramics by spark plasma sintering: Role of annealing. *Ceram Int* 2020, **46**: 15076–15083.
[47] Wurst JC, Nelson JA. Lineal intercept technique for measuring grain size in two-phase polycrystalline ceramics. *J Am Ceram Soc* 1972, **55**: 109–109.
[48] Tsuji K, de Beauvoir TH, Ndayishimiye A, *et al.* Cold sintering of yttria-stabilized cubic bismuth oxide: Conductivity and microstructural evolution of metastable grain boundaries with annealing. *J Appl Phys* 2020, **128**: 215104.
[49] Lungu MV. Effects of dopants and processing parameters on the properties of ZnO–V_2O_5-based varistors prepared by powder metallurgy: A review. *Materials* 2023, **16**: 3725.
[50] Conry B, Harley JB, Tonks MR, *et al.* Engineering grain boundary anisotropy to elucidate grain growth behavior in alumina. *J Eur Ceram Soc* 2022, **42**: 5864–5873.
[51] Asokan T, Iyengar GNK, Nagabhushana GR. Studies on microstructure and density of sintered ZnO-based non-linear resistors. *J Mater Sci* 1987, **22**: 2229–2236.
[52] Chen BH, Wang BW, Gao PZ, *et al.* Effects of raw particle size and annealing on microstructure, electrical and mechanical behaviors of ZnO-based varistors. *J Alloys Compd* 2021, **872**: 159638.
[53] Hsiang HI, Tsai HR, Pithan C. Effects of $Sr(Co,Nb,Ta)O_3$ addition on the defect structures and electrical properties of ZnO-based varistors. *J Mater Chem C* 2022, **10**: 9644–9654.
[54] Bueno PR, Varela JA, Longo E. SnO_2, ZnO and related polycrystalline compound semiconductors: An overview and review on the voltage-dependent resistance (non-ohmic) feature. *J Eur Ceram Soc* 2008, **28**: 505–529.
[55] Lucat C, Martin MP, Debéda-Hickel H, *et al.* Screen-printed varistors: New strategy for high non-linear coefficient. *J Eur Ceram Soc* 2007, **27**: 3883–3886.
[56] Fu ZY, He JJ, Lu JZ, *et al.* Investigation of dielectric relaxation and degradation behavior of two-step sintered ZnO varistors. *Ceram Int* 2019, **45**: 21900–21909.
[57] Xu D, Tang DM, Lin YH, *et al.* Influence of Yb_2O_3 doping on microstructural and electrical properties of ZnO–Bi_2O_3-based varistor ceramics. *J Cent South Univ* 2012, **19**: 1497–1502.
[58] Xu D, Tang DM, Jiao L, *et al.* Effects of high-energy ball milling oxide-doped and varistor ceramic powder on ZnO varistor. *Trans Nonferrous Met Soc China* 2012, **22**: 1423–1431.
[59] Niu JP, She HB, Liu ZY, *et al.* A current-controlled flash sintering processing leading to dense and fine-grained typical multi-element ZnO varistor ceramics. *J Alloys Compd* 2021, **876**: 160124.
[60] Bernik S, Maček S, Ai B. Microstructural and electrical characteristics of Y_2O_3-doped ZnO–Bi_2O_3-based varistor ceramics. *J Eur Ceram Soc* 2001, **21**: 1875–1878.
[61] Li JQ, Tang K, Yang SJ, *et al.* Effects of doping Y_2O_3 on the microstructure and electrical properties of ZnO–Bi_2O_3-based varistor ceramics. *J Electroceram* 2021, **46**: 131–140.
[62] Sze SM. *Physics of Semiconductor Devices*, 2nd edn. New York (USA): John Wiley & Sons, 1981.
[63] Levinson LM, Philipp HR. The physics of metal oxide varistors. *J Appl Phys* 1975, **46**: 1332–1341.
[64] Barsoukov E, Macdonald JR. *Impedance Spectroscopy Theory Experiment, and Applications*, 2nd edn. New York (USA): John Wiley & Sons, 2005.